
TWO-DIMENSIONAL RMSD PROJECTIONS FOR REACTION PATH VISUALIZATION AND VALIDATION

A PREPRINT

 **Rohit Goswami***

Institute IMX and Lab-COSMO

École polytechnique fédérale de Lausanne (EPFL)

Station 12, CH-1015 Lausanne, Switzerland

and

TurtleTech ehf., 107 Reykjavík, Iceland

rgoswami@ieee.org

February 10, 2026

ABSTRACT

Transition state or minimum energy path finding methods constitute a routine component of the computational chemistry toolkit. Standard analysis involves trajectories conventionally plotted in terms of the relative energy to the initial state against a cumulative displacement variable, or the image number. These dimensional reductions obscure structural rearrangements in high dimensions and are often history dependent. This precludes the ability to compare optimization histories of different methods beyond the number of calculations, time taken, and final saddle geometry. We present a method mapping trajectories onto a two-dimension projection defined by a permutation corrected root mean square deviation from the reactant and product configurations. Energy is represented as an interpolated color-mapped surface constructed from all optimization steps using a gradient aware derivative Gaussian Process. This representation highlights optimization trajectories, identifies endpoint basins, and diagnoses convergence concerns invisible in one-dimensional profiles. We demonstrate the framework on a cycloaddition reaction, showing that a machine-learned potential saddle and density functional theory reference lie on comparable energy contours despite geometric displacements, along with the ratification of the visualization for more complex reactions, a grignard rearrangement, and a bicyclobutadiene rearrangement.

Keywords Nudged Elastic Band, Saddle Search Methods, Visualization, Transition States

The first order saddle point, is often the first approximation to understand the reaction kinetics of any system of interest. Starting from two known configurations, a series of configurations connected through fictitious springs, that is, the nudged elastic band method [1] is among the most common. The NEB may be coupled with the climbing image [2] and spring variations [3] with machine learned local accelerations [4–6] and the string family of methods [7–9]. Together, these form the current Pareto optimal forms to find a saddle.

Beyond difficulties of convergence and the intricacies of the initial points chosen, the resulting path histories are best studied through the “eye-ball norm”, wherein manual inspection of the final path, along with a normal mode analysis for the saddle point estimate are considered sufficient. In turn, this means the most common visual plots, are one dimensional “profile” plots. These may show only the final optimized path, against the image number², which obscures any distance measure between the images. Alternatively, a well-known improvement to this involves the cubic Hermite interpolation [2] involving the forces relative to the “reaction coordinate,” defined by the piece-wise sum of the Euclidean distances between intermediate images. The reaction coordinate $s_i = \sum_{j=1}^i \|\mathbf{R}_j - \mathbf{R}_{j-1}\|_2$ depends entirely on the specific path geometry and optimization history. This scalar measure lacks a unique definition and

*Corresponding Author

²e.g. as found in ASE [10]

collapses global geometric information onto a single, arbitrary axis. This dimensional reduction precludes rigorous comparison between trajectories generated by differing algorithms—such as NEB versus Frozen String methods—or even identical algorithms with varying parameters. Furthermore, the one-dimensional projection frequently masks the distinction between numerical instability and physical relaxation into alternative basins, creating ambiguity in the validation of stationary points which costs researchers often days of calculations to clarify.

1 Methodology

We describe the one-dimensional profiles first. Since standard NEB implementations provide discrete images \mathbf{X}_i and energies E_i . To reconstruct a physically consistent energy profile $E(s)$ along the path, we utilize the available force information. We define the discrete reaction coordinate s_i as the cumulative Euclidean distance:

$$s_i = \sum_{j=1}^i \|\mathbf{X}_j - \mathbf{X}_{j-1}\| \quad (1)$$

Instead of simple linear or cubic interpolation, we employ a Piecewise Cubic Hermite Interpolating Polynomial (PCHIP). This method utilizes the tangent forces $F_{\parallel,i}$ to constrain the derivative of the energy surface:

$$\left. \frac{dE}{ds} \right|_{s_i} = -F_{\parallel,i} = -(\mathbf{F}_i \cdot \hat{\tau}_i) \quad (2)$$

where $\hat{\tau}_i$ denotes the unit tangent vector along the path.

1.1 Intrinsic Projection Coordinates

To map the high-dimensional optimization trajectory onto a consistent 2D subspace, we define the projection coordinates (u, v) as the distances from the reactant (\mathbf{R}) and product (\mathbf{P}) reference configurations. To ensure the metric remains robust across automated workflows where atom indexing may vary, we employ a permutation-invariant Root Mean Square Deviation (RMSD) with optimal permutation \mathbf{P} and rotation \mathbf{R} determined via the Iterative Rotations and Assignments (IRA) [11] algorithm. This procedure guarantees unique, invariant coordinates regardless of the initial atom indexing or frame orientation [6]. The discrete optimization steps provide a sparse sampling of this geometric subspace.

For a system with N atoms having positions $\mathbf{X} \in \mathbb{R}^{3 \times N}$, we define the distance metric $d(\mathbf{X}, \mathbf{X}_{\text{ref}})$ as:

$$d(\mathbf{X}, \mathbf{X}_{\text{ref}}) = \min_{\mathbf{Q}, \mathbf{\Pi}} \sqrt{\frac{1}{N} \|\mathbf{X} - \mathbf{Q}\mathbf{X}_{\text{ref}}\mathbf{\Pi}\|_F^2} \quad (3)$$

Here, $\|\cdot\|_F$ denotes the Frobenius norm. $\mathbf{Q} \in SO(3)$ represents the optimal rotation matrix, and $\mathbf{\Pi}$ represents the optimal permutation matrix. We solve for \mathbf{Q} and $\mathbf{\Pi}$ simultaneously. This ensures that the resulting coordinates $(u, v) = (d(\mathbf{X}, \mathbf{R}), d(\mathbf{X}, \mathbf{P}))$ remain invariant to rigid body rotation, translation, and arbitrary atom index labeling.

Unlike principal component analysis (PCA) [12] or t-distributed stochastic neighbor embedding (t-SNE) [13] applied to covariance matrices [14, 15], which require a priori selection of descriptors (e.g., bond lengths, angles, SOAP vectors [16]), RMSD-based projection operates directly on Cartesian coordinates without feature engineering. PCA-based methods popular in machine learning interatomic potential (MLIP) communities presuppose that the dominant variance directions align with chemically meaningful coordinates—an assumption that frequently fails for complex rearrangements involving concerted bond breaking and formation. Similarly, manifold learning techniques like t-SNE and UMAP [17] optimize for local neighborhood preservation but lack the absolute geometric reference frame necessary for quantitative cross-method comparison. The closest estimate involves a data-intensive estimate of local-global distance mappings using the sketchmap [18]. Our endpoint-distance coordinates provide a universal, reaction-agnostic metric that requires no manual intervention or presupposed chemical intuition about the reaction mechanism.

For systems with well-established collective variables—Ramachandran angles for peptides, donor-acceptor distances for proton transfer—such coordinates are likely to naturally provide superior physical insight [19]. However, transition state searches in realistic systems (e.g., catalytic cycles, surface reactions, conformational transitions in drug molecules) rarely afford such clarity. Unlike free energy surface (FES) methods that mandate pre-specification of reaction coordinates,

our approach visualizes arbitrary path based methods post hoc, requiring only the endpoints. This eliminates the circular dependency where one must already understand the mechanism to choose coordinates capable of revealing it.

Our method targets the complementary regime to global PES exploration techniques: we provide geometric validation for individual optimization trajectories ($\approx 10^3$ samples per NEB calculation) rather than exhaustive basin catalogs requiring $\approx 10^6 - 10^9$ samples. Most single NEB calculations involve only $\approx 10^3$ geometries concentrated along a one-dimensional path connecting a single reactant-product pair. This sampling is insufficient and inappropriate for techniques designed to map complete basin connectivity or construct disconnectivity graphs [20]. Our framework instead answers a distinct question: “Did this specific optimization find a physically reasonable barrier topology?” This diagnostic capability proves critical for MLIP validation, where the goal is verifying that a machine-learned potential reproduces the correct transition pathway—not exhaustively cataloging all possible pathways.

1.2 Energy Landscape Projection

The discrete optimization steps provide a sparse, unstructured sampling of the 2D (u, v) domain. To visualize slices of the underlying potential energy landscape $E(u, v)$, in a meaningful way to compare data from disparate calculations, we construct a continuous projection approximating the potential energy surface.

While forces $F = -\nabla_R(E)$ are available from electronic structure calculations in 3N-dimensional Cartesian space, direct projection via the chain rule would require computing $\partial d_{\text{RMSD}}/\partial R$ —a quantity complicated by the minimization over permutations and rotations implicit in the RMSD definition. Instead, we construct synthetic gradients in the 2D projection space by combining the path tangent vector with the available parallel force component.

First, we stabilize the tangent calculation via Savitzky-Golay smoothing of the RMSD coordinates themselves:

$$\tilde{r}_i, \tilde{p}_i = \text{SavGol}(r_i, p_i; \text{window} = 5, \text{poly} = 2) \quad (4)$$

From the smoothed coordinates, we compute the path tangent:

$$\tau_r = \frac{d\tilde{r}}{ds}, \quad \tau_p = \frac{d\tilde{p}}{ds} \quad (5)$$

where the tangent is normalized so $\|\tau\| = 1$. The projected gradient components are then:

$$\nabla_r E = -F_{\parallel} \cdot \tau_r, \quad \nabla_p E = -F_{\parallel} \cdot \tau_p \quad (6)$$

where F_{\parallel} is the force component parallel to the path (column 3 in an eOn .dat file). This construction ensures gradient information respects the local path geometry while remaining tractable to compute from standard NEB output.

From this, among other surface constructions we highlight the Gaussian Process Regression (GPR) with gradient (derivative) information [21–23]. In this instance, construct the energy surface using a gradient-enhanced Inverse Multiquadric (IMQ) kernel:

$$k(\mathbf{x}, \mathbf{x}') = (c^2 + \|\mathbf{x} - \mathbf{x}'\|^2)^{-1/2} \quad (7)$$

where c is a scale parameter controlling the transition from local to global correlation behavior. The IMQ kernel provides several critical advantages over alternatives. Unlike the Matérn family, which exhibits exponential decay, IMQ’s polynomial (r^{-1}) tail behavior enables simultaneous capture of local path features and long-range basin structure—essential for revealing multi-well topologies common in chemical reactions. Compared to squared exponential (RBF) kernels that can over-smooth genuine landscape features, IMQ preserves fine structure while maintaining interpolation stability. The heavy-tailed correlation structure proves particularly effective for NEB trajectories, where data points cluster tightly along the path but the landscape must be extrapolated to surrounding regions.

We augment the standard energy-only covariance matrix with derivative observations. For each sampled point $(x_i, y_i) = (d_{\text{RMSD}}(S_i, R), d_{\text{RMSD}}(S_i, P))$, we include the projected gradients $(\nabla_x E, \nabla_y E)$ computed as described above. This constructs an augmented observation vector $y_{\text{full}} = [E_1, \nabla_x E_1, \nabla_y E_1, E_2, \nabla_x E_2, \nabla_y E_2, \dots]$ with corresponding gradient-augmented kernel blocks [24]:

$$K_{\text{full}} = \begin{bmatrix} k(x_i, x_j) & \nabla_{x'} k(x_i, x_j) \\ \nabla_x k(x_i, x_j) & \nabla_x \nabla_{x'} k(x_i, x_j) \end{bmatrix} \quad (8)$$

where the derivative covariances are computed via automatic differentiation using the JAX library. This derivative information enforces local slope consistency—preventing spurious oscillations between data points—and effectively triples the information content per geometry without additional energy evaluations.

The hyperparameter optimization follows the subset optimization [25] concept from the OT-GPD, here, the points from the final path are used to calculate the length and noise scales, which are subsequently applied while fitting the entire surface. This subsampled approach reduces computational cost from $O(N^3)$ to $O(n^3)$ where $n \ll N$ (typically $n \approx 20$ vs $N \approx 500 - 2000$), while simultaneously improving robustness by isolating hyperparameter learning from transient optimization dynamics.

The resulting interpolated surface enables direct overlay of reference structures (e.g., DFT-optimized saddle points) onto MLIP-generated landscapes. Visual assessment of whether a potential captures qualitatively correct barrier topology becomes possible even when geometric displacements occur—a capability impossible with 1D energy profiles where the reaction coordinate axis itself depends on path geometry. This addresses a critical gap in current MLIP validation workflows.

2 Results

We validate the framework, first contrasting against 1D profiles for the 1,3-dipolar cycloaddition of ethylene and N_2O forming 4,5-dihydro-1,2,3-oxadiazole, a well-studied benchmark reaction for NEB method development [3, 5, 9, 26–28]. Figure 1 compares conventional one-dimensional representations with the two-dimensional RMSD projection for energy-weighted NEB optimization in eOn [29]³ using the PET-OMAT machine-learned potential [30, 31] using Metatomic [26]. The model has been trained on PBE reference data from the Open Materials dataset [32], with full construction details in the associated publication. For the cycloaddition, we contrast this with a saddle optimized from a different NEB calculation using the B3LYP functional in ORCA [3] projected onto the interpolated landscape.

The conventional profiles (Fig.1, bottom) show optimization from an initial barrier of approximately 1.1 eV to a final value near 0.4 eV over 120 steps, with the product lying approximately 0.8 eV below the reactant. The final path appears smooth and well-converged. These representations provide no information about sampling quality or the broader landscape topology.

The two-dimensional RMSD projection (Fig.1, top) provides some more insight. First, sampled structures (black dots) cluster tightly along the converged path, confirming robust single-pathway convergence. Second, the interpolated energy surface displays clear landscape topology: a barrier region (yellow/orange, approximately 0.4eV) separating the reactant basin (upper-left) from the deeper product basin (blue, lower-right). The projection reveals that the ORCA saddle configuration overlaps with the estimate from the MLIP.

To demonstrate robustness on non-trivial topologies, we analyze the Grignard rearrangement of (Z)-2-phenyl-2-((trimethylsilyl)oxy)hex-4-enenitrile [28] and the electrocyclic ring opening of bicyclobutadiene (Figure 2) [9]. Unlike the linear character of the cycloaddition, these reactions proceed through significant geometric turns. The Grignard pathway (Figure 2a) exhibits a curved trajectory where the path tangent rotates nearly 90 degrees in the (RMSD_R , RMSD_P) plane. The 2D projection clearly captures the optimization noise (scattered black points) in the solvent-mediated reactant region, a diagnostic feature lost in scalar reaction coordinate plots, while demonstrating without explicitly needing to study the structures, the fact that they lie on the same energy contour. Similarly, the bicyclobutadiene isomerization (Figure 2b) displays a sharp geometric “elbow” immediately following the transition state. The interpolated surface correctly places the reference Free String Method (mlFSM) saddle [9] within the barrier region of the MLIP. This confirms that the NEB trajectory found the physically relevant saddle despite the complex topology, a validation that remains ambiguous when observing only the image index or scalar reaction coordinate⁴.

Furthermore, this framework provides a unified coordinate system for validating potential energy surfaces against higher-level theory. If these disagree, the relative differences between the saddles would be apparent. For a reaction like the cycloaddition, this is perhaps not very interesting, as both saddles are equally well resolved on the energy surface. The projections could reveal if resulting structures are within comparable energy contours. Such an analysis to check if the energy surface captures the qualitative barrier topology even if the precise saddle geometry differs due to functional sensitivity would be impossible with conventional one-dimensional profiles.

For complete reproduction, the materials archive includes both exact commands, and outputs at the time of submission.

³from <https://eondocs.org>

⁴or in practice, would involve normal mode analysis, barrier heights, RMSD, and visual inspection

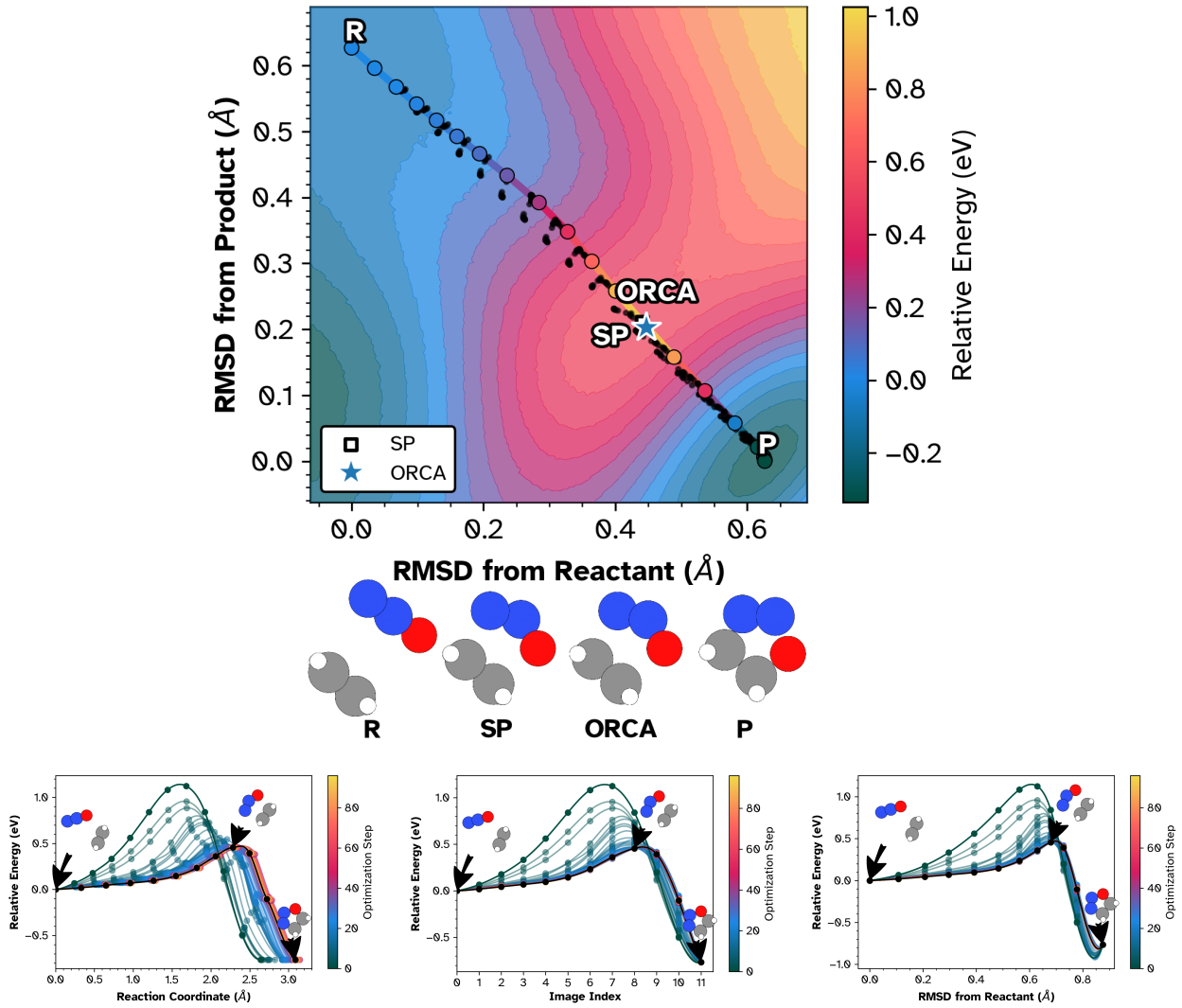


Figure 1: NEB optimization of ethylene + N_2O cycloaddition using the MLIP. **Top:** 2D RMSD projection showing interpolated energy landscape (color), sampled structures (black dots), and converged path (open circles). White star indicates ORCA B3LYP-D3 saddle. **Bottom left:** Energy vs. reaction coordinate. **Bottom center:** Energy vs. image index. **Bottom right:** Energy vs. RMSD from reactant. In all panels, colored curves show optimization progression (dark→light = early→late); final path in black. The 2D projection reveals landscape topology and enables reference structure assessment impossible in 1D profiles.

Conclusion

We presented a coordinate-free visualization method for analyzing reaction path optimization trajectories. By projecting high-dimensional pathways onto a surface defined by permutation-invariant RMSD coordinates, the method reveals geometric and energetic features obscured by standard one-dimensional profiles.

The benchmarks demonstrate the capacity of this representation to distinguish numerical artifacts from physical topology and to study differences in potential energy surfaces, with an eye towards validating machine learning potentials. This visualization enables validation of saddle point searches beyond point comparisons of geometry and the comparison of diverse saddle finding algorithms on a unified geometric basis. Finally, while we focus on double-ended methods here, the $(\text{RMSD}_R, \text{RMSD}_P)$ projection operates independently of the path generation algorithm. One can in principle project histories from single-ended saddle search methods, molecular dynamics, or meta-dynamics onto these intrinsic axes post-hoc to diagnose path quality and hysteresis with a destination basin. Additionally, the relative energy surfaces from multiple machine learning models could also be probed within such a framework.

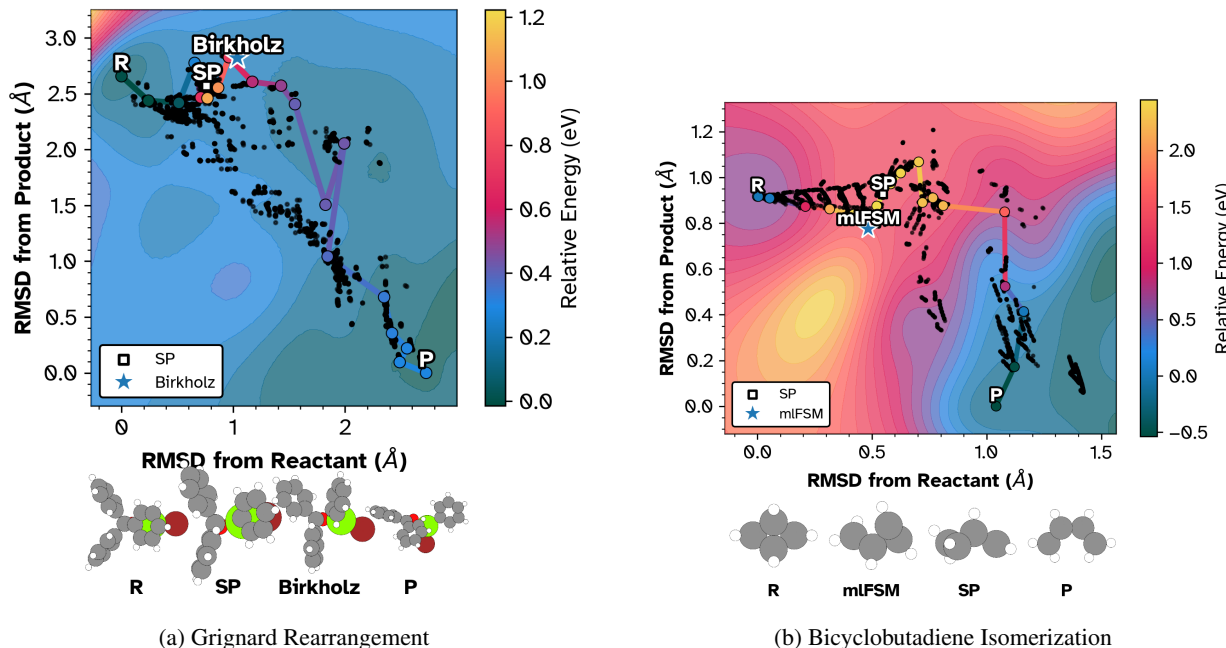


Figure 2: Two-dimensional RMSD projections of complex rearrangement pathways. (a) The Grignard rearrangement of (Z)-2-phenyl-2-((trimethylsilyl)oxy)hex-4-enenitrile exhibits a distinct “turning” mechanism. The projection reveals significant optimization instability (scattered black dots) near the reactant basin that 1D profiles would obscure. The star indicates the reference saddle from Birkholz et al. (b) The conrotatory ring opening of bicyclobutadiene shows a sharp geometric “kink” post-transition state. The projection confirms the machine-learned potential path (circles) faithfully traverses the saddle region identified by the Free String Method (star).

Conflict of Interest

We declare no conflicts of interest.

References

- [1] Hannes Jonsson, Greg Mills, and Karsten W. Jacobsen. Nudged elastic band method for finding minimum energy paths of transitions. In *Classical and Quantum Dynamics in Condensed Phase Simulations*, pages 385–404. World Scientific, June 1998. ISBN 978-981-02-3498-0. doi:10.1142/9789812839664_0016.
- [2] Graeme Henkelman, Blas P. Uberuaga, and Hannes Jónsson. A climbing image nudged elastic band method for finding saddle points and minimum energy paths. *The Journal of Chemical Physics*, 113(22):9901–9904, November 2000. ISSN 0021-9606. doi:10.1063/1.1329672.
- [3] Vilhjálmur Ásgeirsson, Benedikt Orri Birgisson, Ragnar Björnsson, Ute Becker, Frank Neese, Christoph Riplinger, and Hannes Jónsson. Nudged Elastic Band Method for Molecular Reactions Using Energy-Weighted Springs Combined with Eigenvector Following. *Journal of Chemical Theory and Computation*, 17(8):4929–4945, August 2021. ISSN 1549-9618. doi:10.1021/acs.jctc.1c00462.
- [4] Rohit Goswami, Maxim Masterov, Satish Kamath, Alejandro Peña-Torres, and Hannes Jónsson. Efficient implementation of gaussian process regression accelerated saddle point searches with application to molecular reactions, May 2025.
- [5] Olli-Pekka Koistinen, Vilhjálmur Ásgeirsson, Aki Vehtari, and Hannes Jónsson. Nudged Elastic Band Calculations Accelerated with Gaussian Process Regression Based on Inverse Interatomic Distances. *Journal of Chemical Theory and Computation*, 15(12):6738–6751, December 2019. ISSN 1549-9618. doi:10.1021/acs.jctc.9b00692.
- [6] Rohit Goswami, Miha Gunde, and Hannes Jónsson. Enhanced climbing image nudged elastic band method with hessian eigenmode alignment, January 2026.

[7] Baron Peters, Andreas Heyden, Alexis T. Bell, and Arup Chakraborty. A growing string method for determining transition states: Comparison to the nudged elastic band and string methods. *The Journal of Chemical Physics*, 120(17):7877–7886, May 2004. ISSN 0021-9606, 1089-7690. doi:10.1063/1.1691018.

[8] Paul M. Zimmerman. Growing string method with interpolation and optimization in internal coordinates: Method and examples. *The Journal of Chemical Physics*, 138(18):184102, May 2013. ISSN 0021-9606. doi:10.1063/1.4804162.

[9] Jonah Marks and Joseph Gomes. Incorporation of Internal Coordinates Interpolation into the Freezing String Method. *Journal of Chemical Theory and Computation*, November 2025. ISSN 1549-9618. doi:10.1021/acs.jctc.5c01492.

[10] Ask Hjorth Larsen, Jens Jørgen Mortensen, Jakob Blomqvist, Ivano E. Castelli, Rune Christensen, Marcin Dułak, Jesper Friis, Michael N. Groves, Bjørk Hammer, Cory Hargus, Eric D. Hermes, Paul C. Jennings, Peter Bjerre Jensen, James Kermode, John R. Kitchin, Esben Leonhard Kolsbørg, Joseph Kubal, Kristen Kaasbørg, Steen Lysgaard, Jón Bergmann Maronsson, Tristan Maxson, Thomas Olsen, Lars Pastewka, Andrew Peterson, Carsten Rostgaard, Jakob Schiøtz, Ole Schütt, Mikkel Strange, Kristian S. Thygesen, Tejs Vegge, Lasse Vilhelmsen, Michael Walter, Zhenhua Zeng, and Karsten W. Jacobsen. The atomic simulation environment—a Python library for working with atoms. *Journal of Physics: Condensed Matter*, 29(27):273002, June 2017. ISSN 0953-8984. doi:10.1088/1361-648X/aa680e.

[11] Miha Gunde, Nicolas Salles, Anne Hémeryck, and Layla Martin-Samos. IRA: A shape matching approach for recognition and comparison of generic atomic patterns. *Journal of Chemical Information and Modeling*, 61(11):5446–5457, November 2021. ISSN 1549-9596. doi:10.1021/acs.jcim.1c00567.

[12] Gareth James, Daniela Witten, Trevor Hastie, and Robert Tibshirani. *An Introduction to Statistical Learning*, volume 103 of *Springer Texts in Statistics*. Springer New York, New York, NY, 2013. ISBN 978-1-4614-7137-0 978-1-4614-7138-7. doi:10.1007/978-1-4614-7138-7.

[13] Laurens van der Maaten and Geoffrey Hinton. Visualizing Data using t-SNE. *Journal of Machine Learning Research*, 9(Nov):2579–2605, 2008. ISSN ISSN 1533-7928.

[14] Albert Musaelian, Simon Batzner, Anders Johansson, Lixin Sun, Cameron J. Owen, Mordechai Kornbluth, and Boris Kozinsky. Learning local equivariant representations for large-scale atomistic dynamics. *Nature Communications*, 14(1):579, February 2023. ISSN 2041-1723. doi:10.1038/s41467-023-36329-y.

[15] Michele Ceriotti. Unsupervised machine learning in atomistic simulations, between predictions and understanding. *The Journal of Chemical Physics*, 150(15):150901, April 2019. ISSN 0021-9606. doi:10.1063/1.5091842.

[16] Miguel A. Caro. Optimizing many-body atomic descriptors for enhanced computational performance of machine learning based interatomic potentials. *Physical Review B*, 100(2):024112, July 2019. doi:10.1103/PhysRevB.100.024112.

[17] Leland McInnes, John Healy, and James Melville. UMAP: Uniform Manifold Approximation and Projection for Dimension Reduction. *arXiv:1802.03426 [cs, stat]*, December 2018.

[18] Gareth A. Tribello, Michele Ceriotti, and Michele Parrinello. Using sketch-map coordinates to analyze and bias molecular dynamics simulations. *Proceedings of the National Academy of Sciences*, 109(14):5196–5201, April 2012. doi:10.1073/pnas.1201152109.

[19] D. Mandelli and M. Parrinello. A modified nudged elastic band algorithm with adaptive spring lengths. *Journal of Chemical Physics*, 155(7):74103, August 2021. ISSN 0021-9606. doi:10.1063/5.0059593.

[20] David J. Wales. Exploring Energy Landscapes. *Annual Review of Physical Chemistry*, 69(1):401–425, 2018. doi:10.1146/annurev-physchem-050317-021219.

[21] Rohit Goswami, Maxim Masterov, Satish Kamath, Alejandro Pena-Torres, and Hannes Jónsson. Efficient Implementation of Gaussian Process Regression Accelerated Saddle Point Searches with Application to Molecular Reactions. *Journal of Chemical Theory and Computation*, July 2025. doi:10.1021/acs.jctc.5c00866.

[22] K. V. MARDIA, J. T. KENT, C. R. GOODALL, and J. A. LITTLE. Kriging and splines with derivative information. *Biometrika*, 83(1):207–221, March 1996. ISSN 0006-3444. doi:10.1093/biomet/83.1.207.

[23] David Eriksson, Kun Dong, Eric Lee, David Bindel, and Andrew G Wilson. Scaling gaussian process regression with derivatives. In S. Bengio, H. Wallach, H. Larochelle, K. Grauman, N. Cesa-Bianchi, and R. Garnett, editors, *Advances in Neural Information Processing Systems*, volume 31. Curran Associates, Inc., 2018.

[24] Mykel J Kochenderfer and Tim A Wheeler. *Algorithms for Optimization*.

[25] Rohit Goswami and Hannes Jónsson. Adaptive Pruning for Increased Robustness and Reduced Computational Overhead in Gaussian Process Accelerated Saddle Point Searches. *ChemPhysChem*, November 2025. ISSN 1439-7641. doi:10.1002/cphc.202500730.

- [26] Filippo Bigi, Joseph W. Abbott, Philip Loche, Arslan Mazitov, Davide Tisi, Marcel F. Langer, Alexander Goscinski, Paolo Pegolo, Sanggyu Chong, Rohit Goswami, Sofia Chorna, Matthias Kellner, Michele Ceriotti, and Guillaume Fraux. Metatensor and metatomic: Foundational libraries for interoperable atomistic machine learning, August 2025.
- [27] Andrew W. Ruttinger, Divya Sharma, and Paulette Clancy. Protocol for Directing Nudged Elastic Band Calculations to the Minimum Energy Pathway: Nurturing Errant Calculations Back to Convergence. *Journal of Chemical Theory and Computation*, 18(5):2993–3005, May 2022. ISSN 1549-9618. doi:10.1021/acs.jctc.1c00926.
- [28] Adam B. Birkholz and H. Bernhard Schlegel. Using bonding to guide transition state optimization. *Journal of Computational Chemistry*, 36(15):1157–1166, 2015. ISSN 1096-987X. doi:10.1002/jcc.23910.
- [29] Rohit Goswami, Sam Chill, Rye Terrell, Graeme Henkelman, Matthew Welborn, Liang Zhang, Andreas Pedersen, T-Brink, Erik Edelmann, Jean Claude, Alejandro, Sung Hoon Jung, Seyed Alireza Ghasemi, Chemist29, Satishskamath, Maxim, and Via9A. TheochemUI/eOn: V2.9.0.1. Zenodo, February 2026.
- [30] Arslan Mazitov, Filippo Bigi, Matthias Kellner, Paolo Pegolo, Davide Tisi, Guillaume Fraux, Sergey Pozdnyakov, Philip Loche, and Michele Ceriotti. PET-MAD as a lightweight universal interatomic potential for advanced materials modeling. *Nature Communications*, 16(1):10653, November 2025. ISSN 2041-1723. doi:10.1038/s41467-025-65662-7.
- [31] Filippo Bigi, Paolo Pegolo, Arslan Mazitov, and Michele Ceriotti. Pushing the limits of unconstrained machine-learned interatomic potentials, January 2026.
- [32] Luis Barroso-Luque, Muhammed Shuaibi, Xiang Fu, Brandon M. Wood, Misko Dzamba, Meng Gao, Ammar Rizvi, C. Lawrence Zitnick, and Zachary W. Ulissi. Open materials 2024 (OMat24) inorganic materials dataset and models, October 2024.